OE Optical Engineering

RESEARCH PAPER

Mueller polarimetry for quantifying the stress optic coefficient in the infrared

Jeremy Parkinson,[a] Patrick Coronato,[b] Jake Greivenkamp,[b] Quinn Jarecki,[a] Daniel Vukobratovich,[b] and Meredith Kupinski[a,*]

[a]University of Arizona, Wyant College of Optical Sciences, Tucson, Arizona, United States
[b]Raytheon Missiles and Defense, Tucson, Arizona, United States

ABSTRACT. To observe the polarimetric properties of an uncharacterized infrared transmitting material (IRTM) under various mechanical forces, a Mueller matrix (MM) imaging experiment was augmented with a force apparatus. Principal stress fields were computed from both finite element and closed-form models and spatially aligned with images of birefringence. The slope of the linear relationship between birefringence and principal stress difference is the stress optic coefficient. We discussed the advantages of MM polarimetry for stress optic coefficient measurements. First, no assumptions about the sample's optical properties are necessary. Second, experimental deviations from the intended in-plane stress field can be identified. Third, independent pixels, over a small but appreciable range of stress values, can be selected to quantify experimental variation and improve statistical significance. To validate our experimental procedures, an N-BK7 sample was characterized at room temperature and compared with the industry-accepted value of 2.77 $TPa^{-1} \pm 3\%$ at 589.3 nm. To our knowledge, this is the first report on the stress optic coefficient of N-BK7 in the infrared, which was observed as 2.764 ± 0.1526 TPa^{-1}. The IRTM stress optic coefficient was observed to be 1.948 ± 0.1197 TPa^{-1}. Experimental sources of uncertainty are discussed and quantified.

© The Authors. Published by SPIE under a Creative Commons Attribution 4.0 International License. Distribution or reproduction of this work in whole or in part requires full attribution of the original publication, including its DOI. [DOI: 10.1117/1.OE.63.9.094104]

Keywords: polarimetry; stress analysis; photoelasticity; optical metrology; Mueller matrix imaging

Paper 20240030G received Jan. 8, 2024; revised Aug. 7, 2024; accepted Aug. 24, 2024; published Sep. 20, 2024.

1 Introduction

The stress optic coefficient characterizes the linear relationship between the magnitude of induced birefringence and the internal stress of an optical element. Therefore, the stress optic coefficient of a material is useful for anticipating changes in optical properties under various mechanical and thermal operating environments.[1–5] Mueller matrix (MM) polarimetry is a tool for measuring stress optic coefficients that does not require assumptions about the sample's optical properties and can identify experimental deviations from the intended applied force. However, stress optic coefficient measurements do not typically employ MM polarimetry. The simplest and most popular experimental approach is rotation of polarization components to orientations that achieve minimum and maximum transmission.[6–8] These orientations uniquely quantify the stress optic coefficient when the sample is a pure linear retarder. MM polarimetry does not necessitate this assumption because all polarimetric properties of a sample are measured: retardance, diattenuation, and depolarization. The linear retardance assumption can be

*Address all correspondence to Meredith Kupinski, meredith@optics.arizona.edu

violated by out-of-plane stresses due to mounting misalignment and/or force application. The presence of elliptical retardance in an MM measurement can be used to identify these experimental artifacts. Furthermore, the precision of the observed linear retardance can be improved by increasing the quantity of measurements to over-determine the Mueller reconstruction.[9]

For a given loading condition, the induced stress field is expected to be inhomogeneous across the sample. Imaging this birefringence pattern allows for a comparison between the assumed and observed stress patterns. Therefore, imaging the spatial distribution of the MM offers further advantages in quantifying the stress optic coefficient and assessing experimental conditions. The linear birefringence image can be aligned with simulated stress values, thereby eliminating the need to assume uniform stress. Imaging can also identify defects and regions of residual stress within the sample.

Birefringence, also known as double refraction, is the optical property of a material having a refractive index that depends on the polarization and propagation direction of light. When light passes through a birefringent material, it splits into orthogonal polarizations of varying propagation directions. These polarizations experience unique refractive indices, resulting in different optical path lengths (OPDs). The dependence of OPD on polarization is referred to as retardance and can be reported in degrees, radians, lengths, or waves. In this work, linear retardance is reported in units of degrees. The wavelength λ is set to 1550 ± 0.1 nm, and the sample thickness is measured with calipers to within ± 0.025 mm.

Stress from external forces causes deformations in the atomic arrangement of the material. These deformations cause a discernible birefringence to be induced depending upon the mechanical properties of the materials. The birefringence is linearly proportional to the difference in principal stress for small deformations. The induced optic axis is along the line of action of the applied force. Therefore, any light that is not propagating collinearly with the line of action will experience retardance. For small elastic deformations in which Hooke's law holds, the magnitude of stress-induced birefringence, Δn, is given by the simple linear relation $\Delta n = C(\sigma_1 - \sigma_2)$, where C is the stress optic coefficient and σ_1 and σ_2 are the first and second principal stresses, respectively.[1–3,10] Here, the sample is assumed to be in the xy-plane, with light propagating along the z-axis and the line of action along the y-axis. For many common optical materials, the stress optic coefficient is on the order of 10^{-12} Pa^{-1} and is reported in units of inverse terapascals (TPa^{-1}).[2,4,5,7] In this linear regime, plotting the measured birefringence as a function of the difference between the first and second principal stresses provides the stress optic coefficient as the slope.

Experimentally measuring the stress optic coefficient requires a series of retardance measurements at various loading forces. In this work, the stress optic coefficient of an infrared transmitting material (IRTM) at room temperature was measured with a 1550-nm laser source. A 1-in. diameter disk of sample material was diametrically loaded with increasing force, and the spatial distribution of linear retardance was imaged. Both finite element and closed-form analytical models were used to evaluate the stress fields of various loading conditions. A rotating retarder MM imaging polarimeter measured the spatial distribution of linear retardance. The measured retardance was converted to birefringence, and the region of interest (ROI) was aligned with the simulated principal stress field. The stress optic coefficient of the IRTM was measured to be 1.948 ± 0.1197 TPa^{-1}. To test the precision of our stress optic coefficient measurement procedure, a sample of N-BK7 with similar dimensions was measured and compared with industry-accepted values. The stress optic coefficient of N-BK7 at 1550 nm was measured as 2.764 ± 0.1526 TPa^{-1}.[11] The published N-BK7 value measured at 589.3 nm is 2.77 $\text{TPa}^{-1} \pm 3\%$.[8,12]

2 Stress Application and Modeling

Stress fields resulting from applied forces are a well-characterized phenomenon.[13–17] The loading case relevant to this work is a cylinder loaded with a diametrically opposed concentrated force and a plane stress approximation. This approximation is valid when the thickness of the sample under test (SUT) is much smaller than its diameter and the force is distributed along the entire thickness. Furthermore, the z-axis stress is decoupled from x and y for light propagating along the z-axis, allowing the assumption of zero stress in the z-direction.[7] In Cartesian coordinates, the stress fields for a diametrically loaded cylinder are

$$\sigma_{xx} = -\frac{2f}{\pi t}\left(\frac{(r-y)x^2}{((r-y)^2+x^2)^2} + \frac{(r+y)x^2}{((r+y)^2+x^2)^2} - \frac{1}{2r}\right), \tag{1}$$

$$\sigma_{yy} = -\frac{2f}{\pi t}\left(\frac{(r-y)^3}{((r-y)^2+x^2)^2} + \frac{(r+y)^3}{((r+y)^2+x^2)^2} - \frac{1}{2r}\right), \tag{2}$$

$$\tau_{xy} = \frac{2f}{\pi t}\left(\frac{(r-y)^2 x}{((r-y)^2+x^2)^2} - \frac{(r+y)^2 x}{((r+y)^2+x^2)^2}\right), \tag{3}$$

where r is the SUT radius, and f is the loading force in Newtons (N).[13,14,17,18] Generally, when an optic is subjected to compressive forces, the resulting stress increases the refractive index for polarized light oriented parallel with the line of action. Conversely, tensile stresses decrease the index. In this work, the polarization orientation is defined such that horizontal polarization is along the x-direction, which is orthogonal to the line of action under the given loading condition and thus experiences tensile stresses.[4] The refractive index in the y-direction is expected to increase, thereby making this direction the slow axis. The index in the x-direction may decrease slightly or have no observable change, thus making this the fast axis. The index change in the z-direction will have no effect on the incident signal in accordance with the plane stress approximation.[7]

In this work, the stress fields were simulated with both an analytical model and finite element analysis (FEA). Both methods of modeling the expected stress field produce identical results. This redundant modeling effort is done out of an abundance of caution. Figure 1 shows the stress fields for normal [Eqs. (1) and (2)] and shear [Eq. (3)] components from both closed-form expressions and the FEA simulation. The principal stress components are calculated from the normal and shear stress fields

$$\sigma_{1/2} = \frac{\sigma_{xx}+\sigma_{yy}}{2} \pm \sqrt{\left(\frac{\sigma_{xx}-\sigma_{yy}}{2}\right)^2 + \tau_{xy}^2} \quad . \tag{4}$$

Here, σ_1 is the orientation of maximum compressive stress, and σ_2 is the minimum. Therefore, σ_1 is the orientation of the slow axis, and σ_2 is the fast axis. The orientation of σ_1 is

$$\theta_p = \arctan\left(\frac{2\tau_{xy}}{\sigma_{xx}-\sigma_{yy}}\right). \tag{5}$$

Figure 2 shows the principal stresses and orientation of maximum stress from both the closed-form analytical model and the FEA simulation. From these simulations, a linear equation was fit to the difference in principal stress as a function of applied force. This linear equation was used to interpolate stress values at intermediate force values. In Fig. 3, the predicted retardance magnitude and orientation of N-BK7 were computed from the stress models and prior reports of the stress optic coefficient. This prediction is used to validate our experimental methods so that a SUT of unknown stress optic coefficient can be characterized.

3 Near-Infrared Mueller Matrix Imaging System

The near-infrared polarimeter (NIRPOL) primarily comprises a collimated source, reference detector, polarization state generator (PSG), polarization state analyzer (PSA), and camera [see Fig. 4(a)]. The PSA and PSG each contain a static commercial off-the-shelf linear polarizer (LP) and a rotating custom true zero-order $\lambda/3$ waveplate. To remove the source power fluctuation effects, a reference detector is used prior to the PSG. A He-Ne laser is used to ensure all optical elements and each SUT are oriented at normal incidence to the source beam. The camera is an InGaAs detector with an adjustable focal length lens. It is mounted at a 90-deg angle, effectively rotating the measurement frame. A rotation has been applied for all subsequent measurements to orient the line of action vertically. Stress-induced birefringence is usually spatially dependent across a sample.[2] For this reason, the imaging capabilities of NIRPOL are important to select a region of uniform linear retardance magnitude and the expected retardance orientation relative to the line of action (see Fig. 5). Furthermore, any residual stress or manufacturing defects in the material would be observable in the measured retardance distribution. More information on the

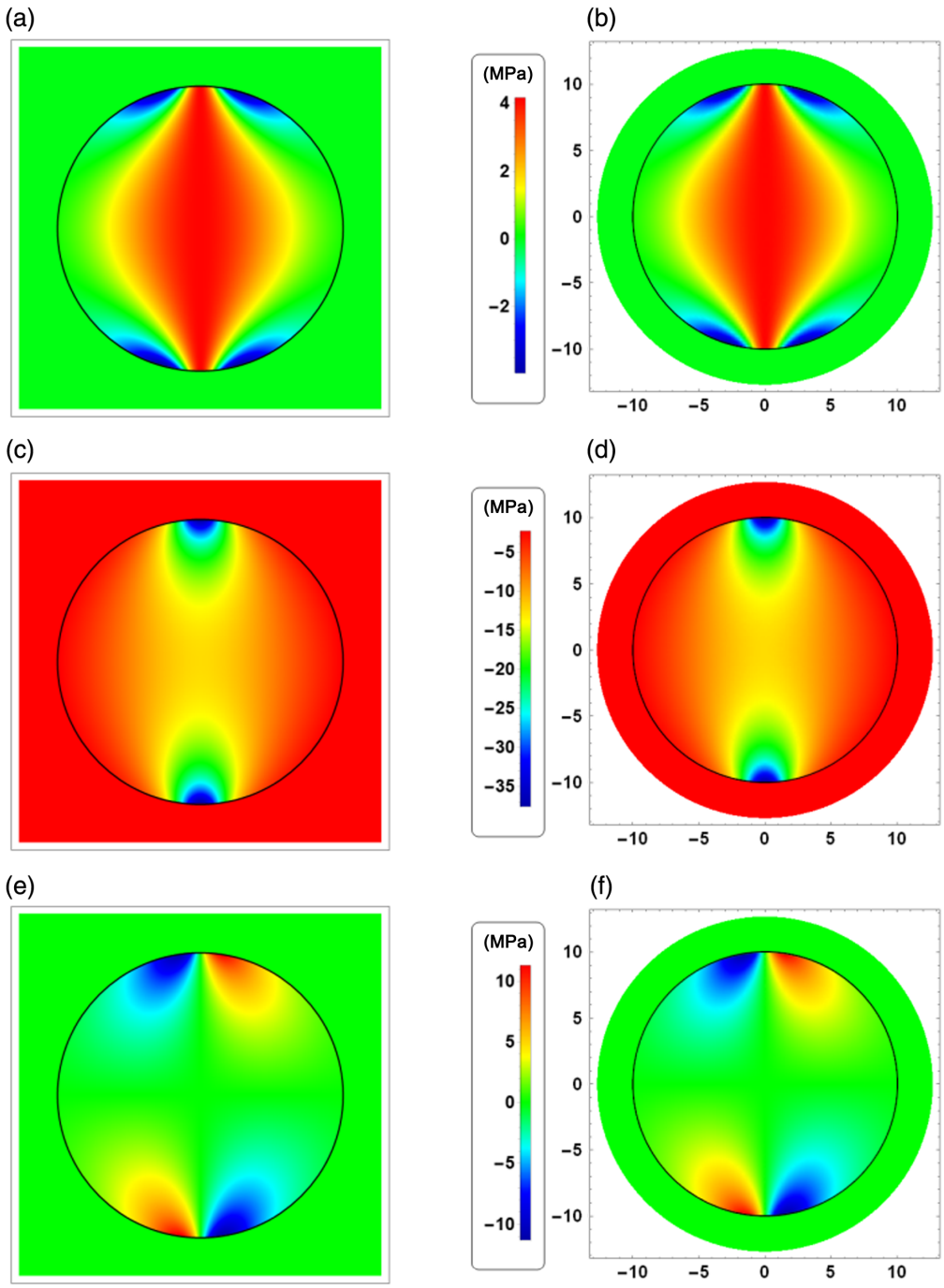

Fig. 1 Comparison of normal and shear stress fields for the closed-form solution (left column) and the FEA model (right column) under 357.75 N loading condition. Distance axes are in millimeters and clipped to exclude extreme values near the contact points. (a) Stress field for σ_{xx}. (b) FEA stress field for σ_{xx}. (c) Stress field for σ_{yy}. (d) FEA stress field for σ_{yy}. (e) Stress field for τ_{xy}. (f) FEA stress field for τ_{xy}.

NIRPOL instrument and component specifications can be found on the open science framework (OSF) project page.[19]

To apply stress during the measurement, a simple fixture was created to support weight and load the sample in compression with increasing force [see Fig. 4(b)]. The sample was compressed between a weight-supporting platform and a precision load cell, which reads the applied force. Some samples were measured at forces as low as 5 N; however, large uncertainties and non-linear effects were observed at such low forces. For this reason, low-magnitude forces were

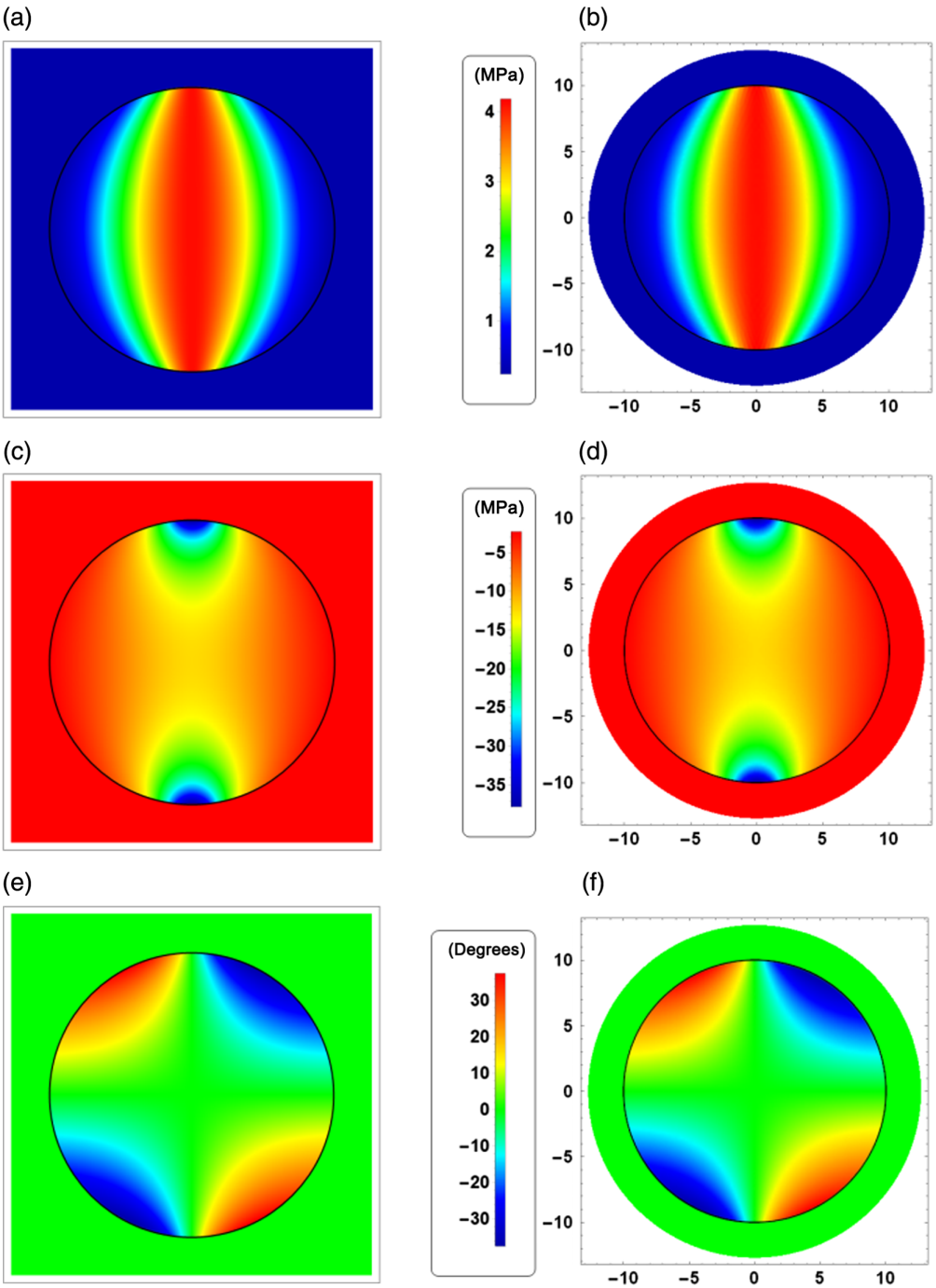

Fig. 2 Comparison of principal stress fields and their orientation for the closed-form solution (left column) and the FEA model (right column) under 357.75 N loading condition. Distance axes are in millimeters and clipped to exclude extreme values near the contact points. (a) Stress field for σ_1. (b) FEA stress field for σ_1. (c) Stress field for σ_2. (d) FEA stress field for σ_2. (e) Principal stress orientation θ_p. (f) FEA principal stress orientation θ_p.

abandoned, leaving five values: 191, 244, 280, 326, and 357N. A zero-load measurement was taken for each SUT to inspect residual stress from the manufacturing process.

4 Polarimetric Data Processing

NIRPOL measures a sequence of 64 images at varying PSG and PSA configurations. The fast axis orientations of the PSG and PSA retarders rotate over the measurement sequence.[20] These 64

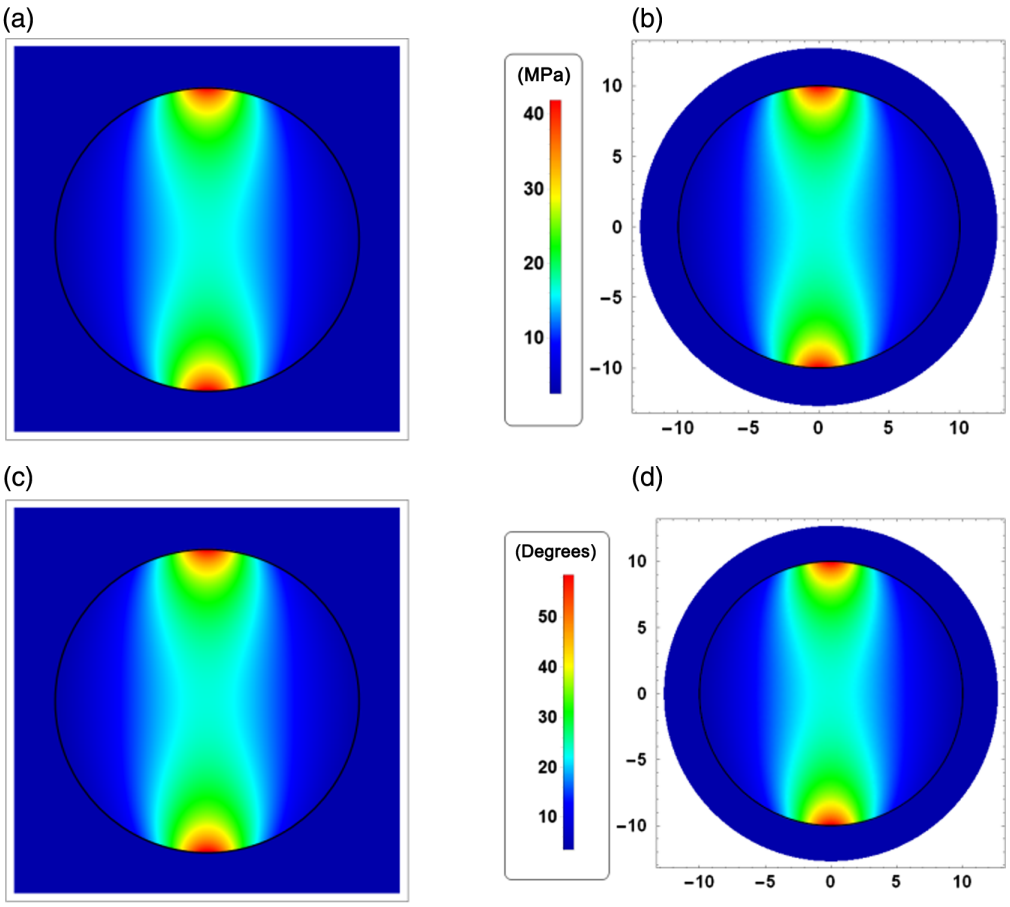

Fig. 3 Principal stress differences and simulated retardance distribution for N-BK7 from closed-form model (left column) and FEA model (right column). The retardance values assume $\lambda = 1550$ nm, $C = 2.77$ TPa^{-1}, and $t = 2.17$ mm. (a) Stress field for $\sigma_1 - \sigma_2$. (b) FEA stress field for $\sigma_1 - \sigma_2$. (c) Simulated retardance, $\delta°$. (d) FEA simulated retardance, $\delta°$.

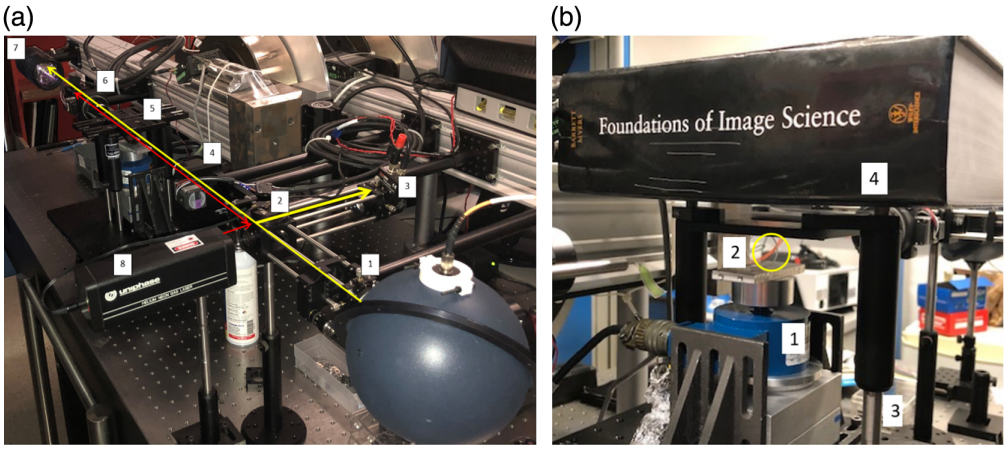

Fig. 4 (a) NIRPOL instrument layout: (1) integrating sphere with adjustable aperture and collimating lens, (2) beamsplitter for reference detection and He-Ne alignment laser, (3) reference detector, (4) PSG, (5) sample space with force application fixture, (6) PSA, (7) InGaAs camera and imaging lens, and (8) He-Ne alignment laser. (b) Fixture for diametric loading: (1) precision load cell for reading force, (2) SUT within the yellow circle, (3) optical posts as guide rails to prevent tilting or twisting, and (4) platform for supporting stress-inducing load.

(a)

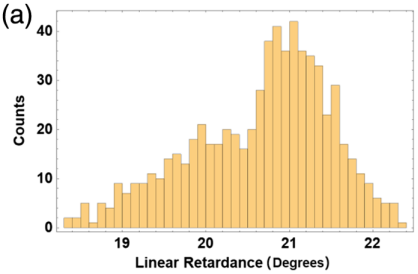

(b)

	Mean	Standard Deviation	Median
Linear Retardance	20.6401	1.9001	21.0041
Retardance Orientation	−61.8022	61.2585	−86.7694
Circular Retardance	0.1171	0.1505	0.1206
Horizontal Retardance	−20.4707	1.9344	−20.8747
45-deg Retardance	−1.9044	1.7916	−1.8380
Retardance Magnitude	20.6410	1.8998	21.0052

Fig. 5 (a) Histogram of ROI linear retardance: histogram of linear retardance within a red circular ROI of 673 pixels in Fig. 10. (b) ROI retardance statistics: statistics of the retardance components. The total retardance magnitude is 20.6401 deg and the linear retardance is 20.6410 deg. Therefore, the plane stress approximation is employed to neglect circular retardance in the stress optic coefficient analysis.

measurements create a system of linear equations that relate the images to the 16 MM elements. The pseudo-inverse of this over-determined linear system reconstructs the MM. For the n'th measurement in the sequence of 64 measurements, the MM of the PSG and PSA are $\mathbf{G}_n = \mathbf{LR}(n \times 5.625 + \theta_g, \delta_g)\mathbf{LP}(0)$ and $\mathbf{A}_n = \mathbf{LP}(\theta_{\mathrm{LP}})\mathbf{LR}(n \times 5.625 \times 4.91 + \theta_a, \delta_a)$. Here, the MM of an ideal linear polarizer is $\mathbf{LP}$, and $\mathbf{LR}(\theta, \delta)$ is a linear retarder with θ fast axis and δ magnitude. The orientation of the PSG linear polarizer is 0 deg by definition and defines the frame of reference. All subsequent axis orientations are defined relative to this axis. The orientation of the PSA linear polarizer is θ_{LP}. The fast axis orientations for the PSA and PSG retarders prior to rotation (i.e., $n = 0$) are denoted θ_a and θ_g, respectively. The PSA and PSG retardance magnitudes are given by δ_a and δ_g, respectively. The PSG retarder rotates 5.625 deg between n and $n + 1$ of the measurement sequence. The PSA retarder rotates 4.91 times the rate of the PSG retarder or 27.62 deg among consecutive measurements.

4.1 Polarimetric Calibration

In the lab frame of reference, the LP transmission axis for the PSG is approximately horizontal or parallel to the optical bench depicted in Fig. 4(a). The precise orientation of the LP is not important, as it defines 0 deg for the experiment. The linear polarizer of the analyzer is aligned with its transmission axis parallel to the PSG LP but not strictly defined as 0 deg to allow for error correction in calibration. Both retarder fast axes at $n = 0$ are aligned to be parallel to the PSG LP transmission axis but also left as a calibration fit parameter to allow for alignment correction. The waveplates are custom true zero-order $\lambda/3$ achromatic elements with a design wavelength of 1550 nm. The retardance magnitude of these elements is also a calibration fit parameter. A sample inserted between the PSA and PSG yields an n'th configuration given by $\mathbf{M}_n = \mathbf{A}_n\mathbf{M}\mathbf{G}_n$, where $\mathbf{M}$ is the MM of the sample. The instrument is calibrated by measuring air, which is expected to produce an MM approximately equal to an identity matrix, and thus, deviations from unity are attributed to instrumental errors.[2,9,20] A least squares fit is performed to calculate $\theta_{\mathrm{LP}}, \theta_a, \theta_g, \delta_a$ and δ_g. Alternate calibration techniques involve the measurement of a sample with known diattenuation or known retardance.[21] This eigenvalue calibration approach provides several advantages, most notably, a functional form of the PSA and PSG is not required. Calibration using a least squares fit to air is limited by the assumed PSA and PSG models, which would be violated by finite diattenutation of the polarizers, component inhomogeneity, and shift-variant polarization aberrations of the imaging optics.

4.2 Linear Retardance Analysis

Lu–Chipman decomposition is performed on the measured Muller matrix to express it as a compound element of pure depolarization ($\mathbf{M}_\Delta$), pure retardance ($\mathbf{M}_R$), and pure diattenuation ($\mathbf{M}_D$), in the order-dependent sequence of $\mathbf{M} = \mathbf{M}_\Delta\mathbf{M}_R\mathbf{M}_D$.[22] Other MM decomposition methods are available, and the appropriate physical assumptions can dictate a choice.[23] Stress-induced birefringence is expected to produce only linear retardance so the simplicity of the Lu–Chipman decomposition is employed. Figure 5 shows that the circular retardance of the SUT is two orders of magnitude lower than the linear retardance. Therefore, the total retardance is assumed to be

strictly linear retardance and is calculated from only the horizontal and 45-deg retardance components, $\delta = \sqrt{\delta_H^2 + \delta_{45}^2}$.

The total retardance magnitude is repeatedly computed from three separate trials for each force magnitude. To calculate the sample statistics on birefringence, the retardance mean and standard deviation within the ROI are averaged over the three trials

$$\overline{\delta} \pm \varepsilon_{\overline{\delta}} = \frac{1}{3}\sum_{k=1}^{3}\delta_k \pm \sqrt{\frac{1}{3}\sum_{k=1}^{3}(\varepsilon_k)^2}. \tag{6}$$

Here, δ_k and ε_k are the mean and standard deviation of linear retardance in a selected region for the k'th trial, respectively. To simplify the propagation of birefringence error, the retardance is converted from degrees to waves

$$\delta_w \pm \varepsilon_{\delta_w} = \frac{\overline{\delta}}{360} \pm \frac{\varepsilon_{\overline{\delta}}}{360} \tag{7}$$

and then to length

$$\delta_\lambda \pm \varepsilon_{\delta_\lambda} = \delta_w\lambda \pm \delta_\lambda\sqrt{\left(\frac{\varepsilon_{\delta_w}}{\delta_w}\right)^2 + \left(\frac{\varepsilon_\lambda}{\lambda}\right)^2}, \tag{8}$$

where δ_λ is the retardance in length, and ε_λ is the uncertainty in wavelength, set to 0.1 nm in this work. Finally, the average birefringence and standard deviation are

$$\Delta n \pm \varepsilon_{\Delta n} = \frac{\delta_\lambda}{t} \pm \Delta n\sqrt{\left(\frac{\varepsilon_{\delta_\lambda}}{\delta_\lambda}\right)^2 + \left(\frac{\varepsilon_t}{t}\right)^2}. \tag{9}$$

4.3 N-BK7 MM Images

The MM image of a 2.17-mm-thick N-BK7 under a 357.75-N compressive force is shown in Fig. 6. The MM is decomposed, and linear retardance is extracted following the methods outlined in Sec. 4.2. Figure 7 shows the depolarizer, retarder, and diattenuator matrices given by the Lu–Chipman decomposition. Here, the depolarizer and diattenuator matrices are proportional to an

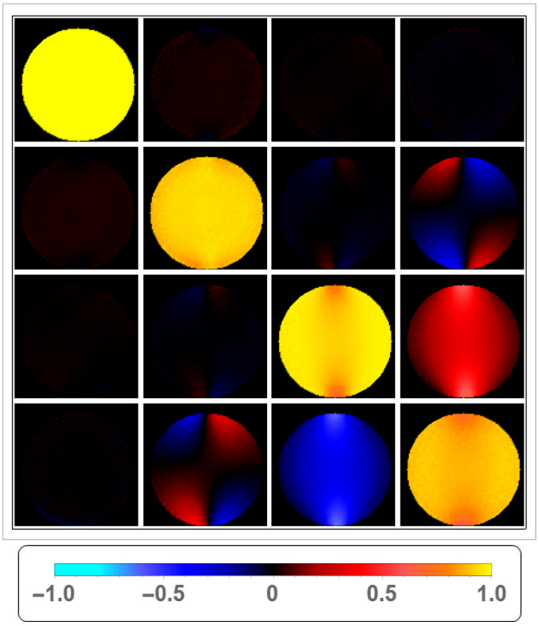

Fig. 6 Normalized MM image of uncoated N-BK7 at 357.75N of force in NIRPOL polarimeter. The line of action is approximately vertical and centered on the SUT.

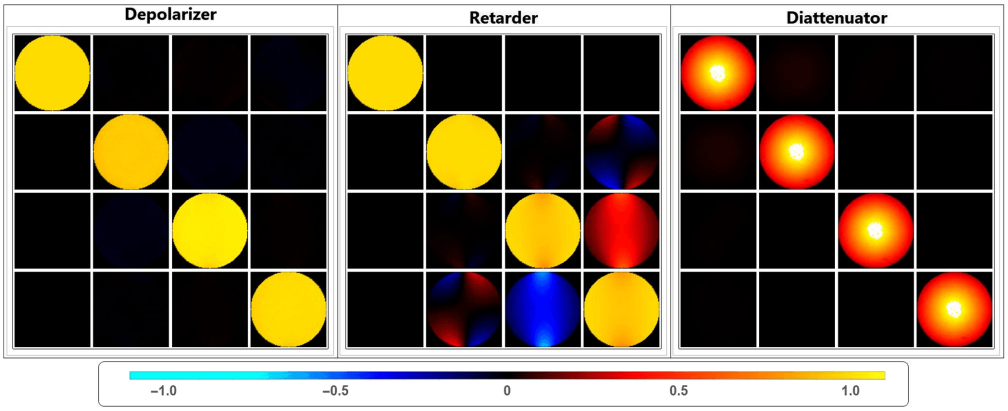

Fig. 7 Lu–Chipman decomposition on the measured MM images from Fig. 6.

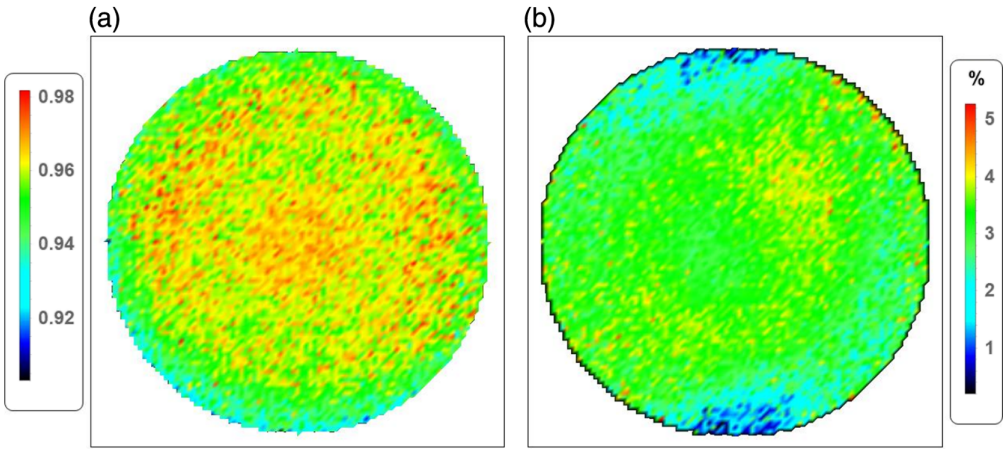

Fig. 8 (a) Depolarization index extracted from the pure depolarizer matrix where a value of 1.0 indicates a non-depolarizing element. (b) Diattenuation magnitude from the pure diattenuator MM in Fig. 7.

identity matrix. This decomposition indicates that the stressed sample's depolarization and diattenuation are negligible. The MM in the vicinity of the contact points is approximately a quarter-wave linear retarder with a horizontal fast axis. The loading force is applied in a vertical direction. Therefore, the slow axis is expected to be vertical. Depolarization and diattenuation in the MM images are neglected in the stress optic coefficient computation. Figure 8 reports the spatial distribution of these values where the average diattenuation is ≈3% and the average depolarization index is ≈96% around the SUT edge.

4.4 Spatial Alignment of Stress to Retardance

Extracting the stress optic coefficient requires precise alignment of the simulated stress fields with the retardance images. Both the measured retardance and principal stress difference are smoothly varying patterns that lack strong features. The alignment was performed manually in two steps. The first step was translating the central values of the three independent trials. As the SUT was mounted and unmounted among trials, the adjustments among them were restricted to translations only. Images were considered properly translated when the variation of the mean image was minimized and uniform. Figures 9 and 10 show the measured retardance for N-BK7 under 357N of loading force for untranslated and translated images, respectively.

The next alignment step was scaling the simulated stress patterns to match the pixel dimension of the retardance images. This unitless scale factor was simply determined as the ratio of pixel quantities between the SUT radius and the half-width of the entire image. The scale factor either compresses or expands the stress pattern to match a given retardance image. The figure of merit for the scale factor was uniformity of the stress optic coefficient image within the red

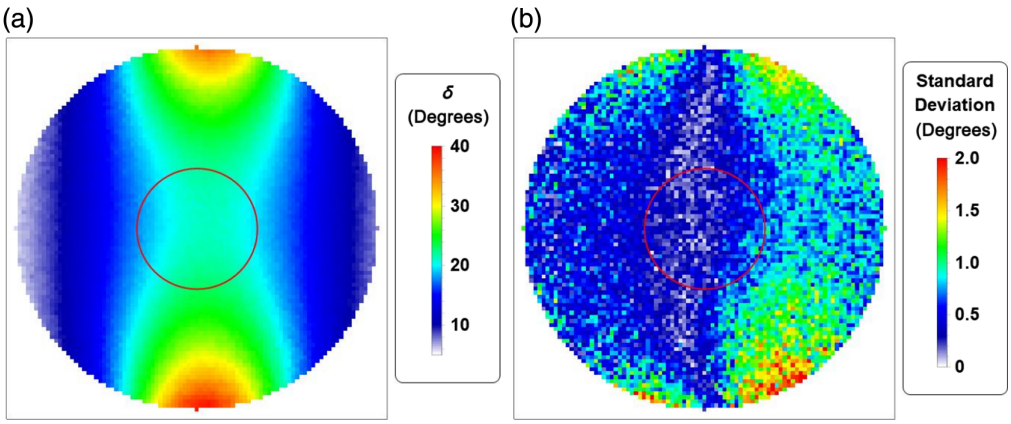

Fig. 9 N-BK7 retardance images before translation. (a) Mean retardance and (b) standard deviation over three independent trials that were mounted and unmounted. The mean image is noticeably off-center, and the standard deviation is less uniform compared with the translated results in Fig. 10.

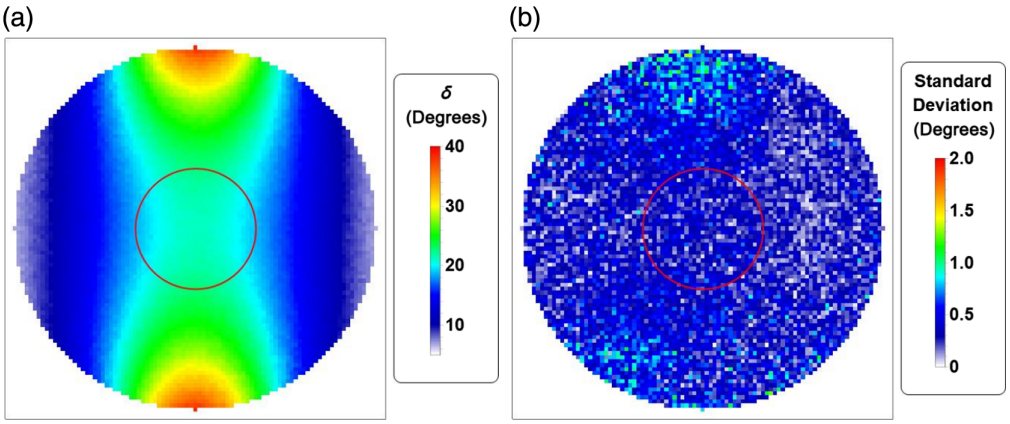

Fig. 10 N-BK7 retardance images after translation. (a) Mean retardance and (b) standard deviation over three independent trials.

circular ROI. Results of improper stress field scaling on stress optic coefficient images are presented in Fig. 11. When the stress field is over-scaled, lower stress values from the central region of the stress field are mapped to larger retardance values, producing a concave-up pattern along the line of action with a minimum at the center of the SUT, as shown in Fig. 11(a). When the stress field is under-scaled, larger stress values from the contact region of the stress field are mapped to smaller retardance values, producing a concave-down pattern along the line of action with a maximum at the center of the SUT, as shown Fig. 11(b).

The stress optic coefficient images with properly aligned intermediate images and stress field are presented in Fig. 12 for N-BK7. An ROI near the center was chosen for analysis due to the slowly varying stress magnitude, which offers less sensitivity to alignment between the measured retardance and the simulated stress. Furthermore, NIRPOL's collimation produces a Gaussian illumination profile, thus lowering the polarimetric dynamic range near the edges of the illuminated region and decreasing SNR in this area. The red circular ROI in Fig. 12 shows higher uniformity and lower variance in the stress optic image.

The 673 ROI pixels are plotted at five color-coded loading forces in Fig. 13 to calculate the stress optic coefficient from linear regression. The R-squared coefficient between the principal stress differences and the birefringence is 0.9961, which indicates excellent agreement with a linear model. The slope of the linear fit produces a stress optic coefficient of 2.764 ± 0.1526 TPa^{-1}, which is within the value reported by Schott of 2.77 TPa^{-1} $\pm$ 3% as measured at 589.3 nm.

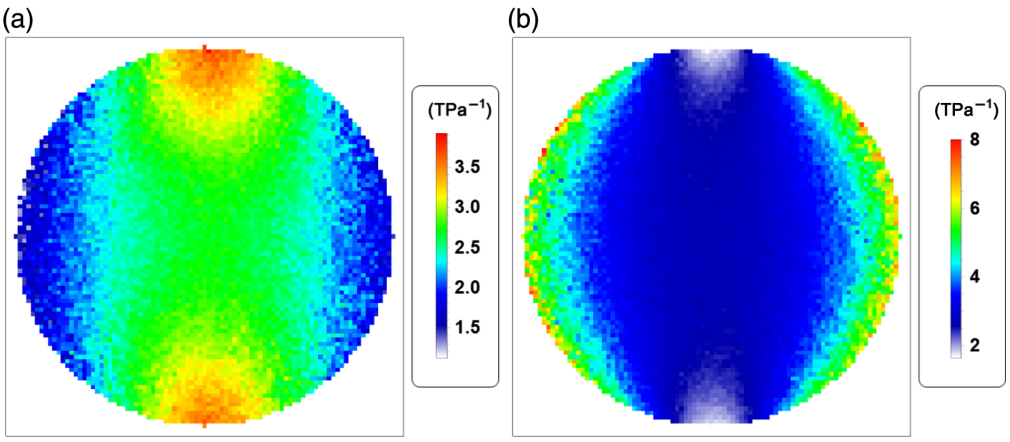

Fig. 11 Stress optic coefficient images. (a) C with over-scaled stress field: the stress field that has been stretched beyond the SUT dimensions. (b) C with under-scaled stress field: the stress field has been compressed smaller than the SUT dimensions. The line of action is vertical, and the high contact point stress is misaligned out of the field of view in panel (a) and too close to the center in panel (b).

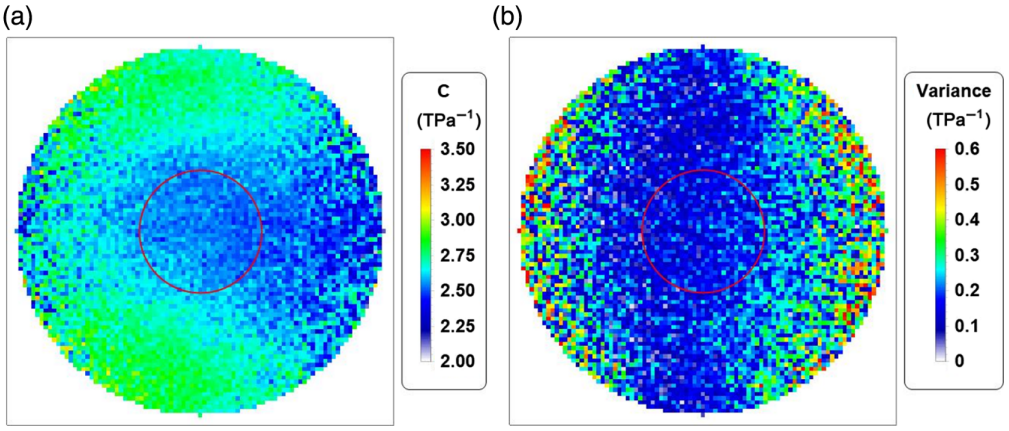

Fig. 12 (a) Mean value and (b) standard deviation for the stress optic coefficient of the N-BK7. The red circular ROI is used for the linear fit analysis in Fig. 13. This ROI is more uniform with lower variance compared with the SUT edges.

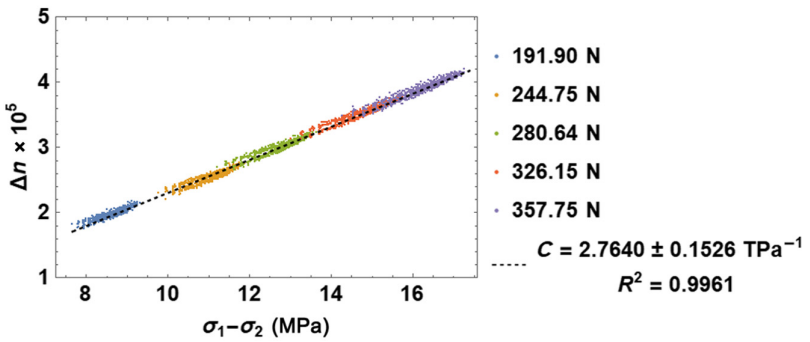

Fig. 13 N-BK7 birefringence versus principal stress difference within the red circular ROI in Fig. 12. Data are averaged over three independent trials and five loading forces, which are color-coded. The slope of the linear fit produces a stress optic coefficient of 2.764 $\pm$ 0.1526 TPa^{-1}, which is within the value reported by Schott of 2.77 TPa^{-1} $\pm$ 3% as measured at 589.3 nm.

5 IRTM Results

The stress optic coefficient of the IRTM sample has not been previously characterized. After the N-BK7 validation experiment, the same procedures were repeated, and the IRTM birefringence

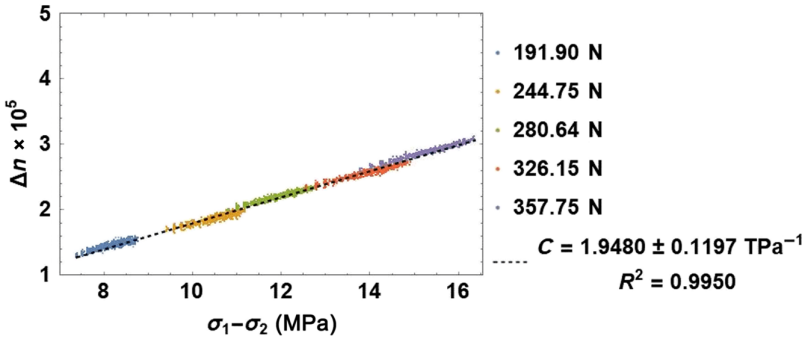

Fig. 14 IRTM birefringence versus principal stress difference within the red circular ROI in Fig. 15. Data are averaged over three independent trial runs and five loading forces, which are color-coded. The slope of the linear fit produces a stress optic coefficient of 1.9480 ± 0.1197 TPa^{-1}.

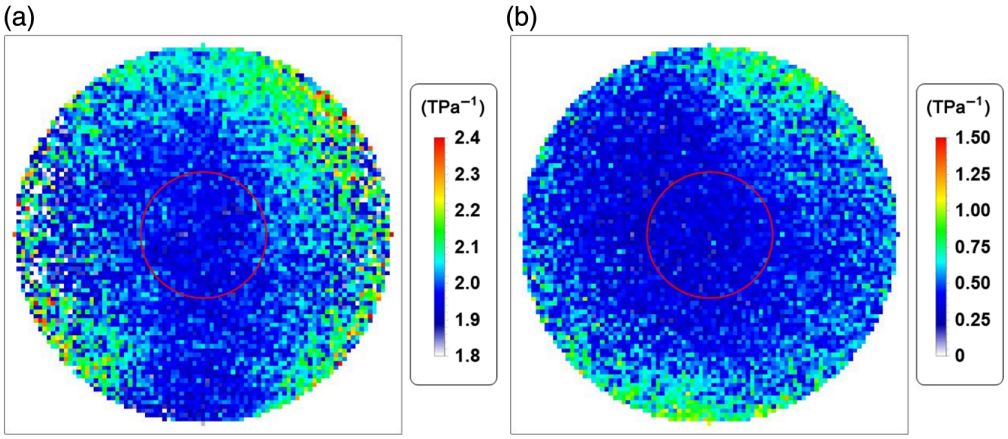

Fig. 15 Images of the IRTM stress optic coefficient. (a) Mean value and (b) standard deviation of C for the IRTM. The red circular ROI is used for the linear fit analysis in Fig. 14.

versus principal stress difference is reported in Fig. 14. For both N-BK7 and IRTM, the R-squared values exceed 0.99, indicating the expected linear relationship. An IRTM stress optic coefficient was produced by repeating this linear fit for each pixel (see Fig. 15).

6 Conclusions and Future Work

This work was conducted to observe the stress optic coefficient of an unstudied IRTM. The stress optic coefficient is vital for anticipating the optical properties of a material in various mechanical and thermal operating environments. To validate our experimental methods, the stress optic coefficient of N-BK7 was measured at 1550 nm and was within the uncertainty of Schott's reported value measured at 589.3 nm. To our knowledge, this is the first report on the infrared stress optic coefficient of N-BK7. The spectral invariance of the N-BK7 stress optic coefficient validates the experimental methods and force apparatus developed to characterize the unstudied IRTM. The IRTM stress optic coefficient was measured to be 1.948 ± 0.1197 TPa^{-1}.

The following three advantages for MM imaging polarimetry to quantify the stress optic coefficient have been demonstrated: assumptions of pure linear retardance were not required. Small effects on the measurement due to depolarization and diattenuation were disregarded using a MM decomposition. Second, a comparison between the expected and observed stress fields was used to align the images and select a region with low stress variation. Any unexpected stress due to out-of-plane stresses from mounting or manufacturing defects can also be identified. Finally, independent pixels from the aligned retardance image, over a small but appreciable range of stress values, were used to quantify experimental variation and improve statistical significance of the reported stress optic coefficient.

Code and Data Availability

Measurements for the N-BK7 sample are available on the polarization lab OSF web page.[19,24] The code to read in the raw Mueller matrix can also be found in the site wiki.[24] Data for IRTM samples are not shared due to ITAR restrictions.

References

1. H. Mueller, "Theory of photoelasticity in amorphous solids," *Physics* **6**(6), 179–184 (1935).
2. R. A. Chipman, W.-S. Tiffany Lam, and G. Young, *Polarized Light and Optical Systems*, CRC Press (2018).
3. H. Mueller, "The theory of photoelasticity," *J. Am. Ceram. Soc.* **21**(1), 27–33 (1938).
4. D. Vukobratovich and P. Yoder, *Fundamentals of Optomechanics*, CRC Press (2018).
5. K. B. Doyle and W. M. Bell, "Thermo-elastic wavefront and polarization error analysis of a telecommunication optical circulator," *Proc. SPIE* **4093**, 18–27 (2000).
6. *Standard Test Method for Measurement of Glass Stress–Optical Coefficient*, ASTM International, West Conshohocken, Pennsylvania (2020).
7. R. D. Mindlin, "A review of the photoelastic method of stress analysis. I," *J. Appl. Phys.* **10**(4), 222–241 (1939).
8. S. Glass, "TIE-27: stress in optical glass," https://www.schott.com/en-us/products/optical-glass-p1000267/downloads (accessed 1 August 2024).
9. J. S. Tyo, "Design of optimal polarimeters: maximization of signal-to-noise ratio and minimization of systematic error," *Appl. Opt.* **41**(4), 619–630 (2002).
10. R. C. Sampson, "A stress-optic law for photoelastic analysis of orthotropic composites," *Exp. Mech.* **10**, 210–215 (1970).
11. J. Parkinson et al., "Mueller polarimetry for quantifying the stress optic coefficient in the infrared," *Proc. SPIE* **12690**, 126900C (2023).
12. S. Glass, "Data sheet, Schott N-BK7," https://www.schott.com/en-us/products/optical-glass-p1000267/downloads (accessed 1 August 2024).
13. W. C. Young and R. G. Budynas, *Roark's Formulas for Stress and Strain*, MacGraw-Hill International Edition, McGraw Hill LLC (2001).
14. A. Freddi, G. Olmi, and L. Cristofolini, "Experimental stress analysis for materials and structures," in *Stress Analysis Models for Developing Design Methodologies, Series in Solid and Structural Mechanics*, p. 498, Springer (2015).
15. A. C. Yiannopoulos, "A general formulation of stress distribution in cylinders subjected to non-uniform external pressure," *J. Elast.* **56**, 181–198 (1999).
16. A. M. Beckley, *Polarimetry and Beam Apodization Using Stress-Engineered Optical Elements*, University of Rochester (2012).
17. K. Ramesh and K. Shins, "Stress field equations for a disk subjected to self-equilibrated arbitrary loads: revisited," *Granular Matter* **24**(2), 1434–7636 (2022).
18. P. S. Theocaris and E. E. Gdoutos, *Matrix Theory of Photoelasticity*, Springer Series in Optical Sciences, Springer-Verlag (1979).
19. M. K. Kupinski, J. C. Parkinson, and Q. Jarecki, "Near-infrared Mueller matrix imaging polarimeter (NIRPOL)," (2024).
20. R. M. A. Azzam, "Photopolarimetric measurement of the Mueller matrix by Fourier analysis of a single detected signal," *Opt. Lett.* **2**(6), 148 (1978).
21. E. Compain, S. Poirier, and B. Drevillon, "General and self-consistent method for the calibration of polarization modulators, polarimeters, and Mueller-matrix ellipsometers," *Appl. Opt.* **38**(16), 3490–3502 (1999).
22. R. A. Chipman and S.-Y. Lu, "Decomposition of Mueller matrices," *Proc. SPIE* **3120**, 385–396 (1997).
23. N. Ortega-Quijano and J. L. Arce-Diego, "Mueller matrix differential decomposition," *Opt. Lett.* **36**(10), 1942–1944 (2011).
24. M. K. Kupinski et al., "Polarization lab," (2024).

Biographies of the authors are not available.